TMDs as a platform for spin liquid physics: A strong coupling study of twisted bilayer WSe₂

Dominik Kiese, Yuchi He, Ciarán Hickey, et al.

COLLECTIONS

Paper published as part of the special topic on Moire Materials

View Online   Export Citation   CrossMark

ARTICLES YOU MAY BE INTERESTED IN

p-type ZnO for photocatalytic water splitting
APL Materials **10**, 030901 (2022); https://doi.org/10.1063/5.0083753

Direct STM measurements of R-type and H-type twisted MoSe₂/WSe₂
APL Materials **10**, 031107 (2022); https://doi.org/10.1063/5.0084358

On the concentration dependence of sound attenuation in aqueous suspensions of silt- and sand-sized sediment: A compilation and analysis of the available data
JASA Express Letters **2**, 036002 (2022); https://doi.org/10.1121/10.0009830

TMDs as a platform for spin liquid physics: A strong coupling study of twisted bilayer WSe$_2$

View Online Export Citation CrossMark

Dominik Kiese,[1] (ID) **Yuchi He,**[2] (ID) **Ciarán Hickey,**[1] (ID) **Angel Rubio,**[3,4,5,a)] (ID) **and Dante M. Kennes**[2,3,b)] (ID)

AFFILIATIONS

[1] Institute for Theoretical Physics, University of Cologne, 50937 Cologne, Germany

[2] Institut für Theorie der Statistischen Physik, RWTH Aachen University and JARA-Fundamentals of Information Technology, 52056 Aachen, Germany

[3] Max Planck Institute for the Structure and Dynamics of Matter and Center for Free Electron Laser Science, Luruper Chaussee 149, 22761 Hamburg, Germany

[4] Center for Computational Quantum Physics, Simons Foundation Flatiron Institute, New York, New York 10010, USA

[5] Nano-Bio Spectroscopy Group, Departamento de Fisica de Materiales, Universidad del País Vasco, UPV/EHU, 20018 San Sebastián, Spain

Note: This paper is part of the Special Topic on Moire Materials.
a) Electronic mail: angel.rubio@mpsd.mpg.de
b) Author to whom correspondence should be addressed: dante.kennes@rwth-aachen.de

ABSTRACT

The advent of twisted moiré heterostructures as a playground for strongly correlated electron physics has led to a plethora of experimental and theoretical efforts seeking to unravel the nature of the emergent superconducting and insulating states. Among these layered compositions of two-dimensional materials, transition metal dichalcogenides are now appreciated as highly tunable platforms to simulate reinforced electronic interactions in the presence of low-energy bands with almost negligible bandwidth. Here, we focus on the twisted homobilayer WSe$_2$ and the insulating phase at half-filling of the flat bands reported therein. More specifically, we explore the possibility of realizing quantum spin liquid (QSL) physics on the basis of a strong coupling description, including up to second-nearest neighbor Heisenberg couplings J_1 and J_2 as well as Dzyaloshinskii–Moriya (DM) interactions. Mapping out the global phase diagram as a function of an out-of-plane displacement field, we indeed find evidence for putative QSL states, albeit only close to SU(2) symmetric points. In the presence of finite DM couplings and XXZ anisotropy, long-range order is predominantly present with a mix of both commensurate and incommensurate magnetic phases.

I. INTRODUCTION

Twisted moiré materials, such as the prominent magic-angle twisted bilayer graphene (tBG), have recently been established as a new platform to study many-body electron physics.[1–27] The key mechanism promoting strongly enhanced electronic correlations is the formation of large moiré unit cells hosting low-energy bands with an extremely narrow bandwidth.[28–30] These flat bands have been shown to give rise to exotic low temperature phase diagrams featuring superconducting and insulating states while offering a high degree of experimental control,[5] e.g., over twist angle and doping.

Recently, twisted bilayer transition metal dichalcogenides (tTMDs) have moved to the center of experimental attention as a tunable platform to simulate electronic many-body states.[31–41] The decisive difference between tBG and tTMDs is the reduction in effective degrees of freedom in going from the former to the latter, allowing for the construction of simplified microscopic Hamiltonians, such as generalized Hubbard models, more amenable to (numerical) quantum many-body methods.[35,36,42,43]

Here, we consider a specific TMD bilayer, twisted WSe$_2$ (tWSe$_2$), for which a correlated insulating phase at half-filling of the flat bands has recently been reported.[31,32] These results have

triggered corollary theoretical activity in deciphering the ground state phase diagram of the effective strong coupling Hamiltonian,[44,45] where the full rotation symmetry of the underlying triangular superlattice is broken down to C_3 by an anisotropic modulation of the spin couplings. The latter is parameterized by a phase ϕ inherited from the respective Hubbard model and can be tuned by an out-of-plane displacement field V_z. Notably, there is evidence from microscopic considerations[44] that large values of $|V_z| > 50$ meV support the emergence of second-nearest

neighbor, SU(2) symmetric Heisenberg exchange interactions. For the pure triangular lattice Heisenberg model, these are believed to undermine magnetic order in favor of a spin liquid ground state,[46–50] and as such, the intriguing possibility of realizing exotic phases in the exceptionally tunable experimental setup provided by twisted TMDs remains an interesting research direction. If experimentally realized, this would add elusive spin liquid states to the list of phases of matter accessible by controlled moiré engineering.[5]
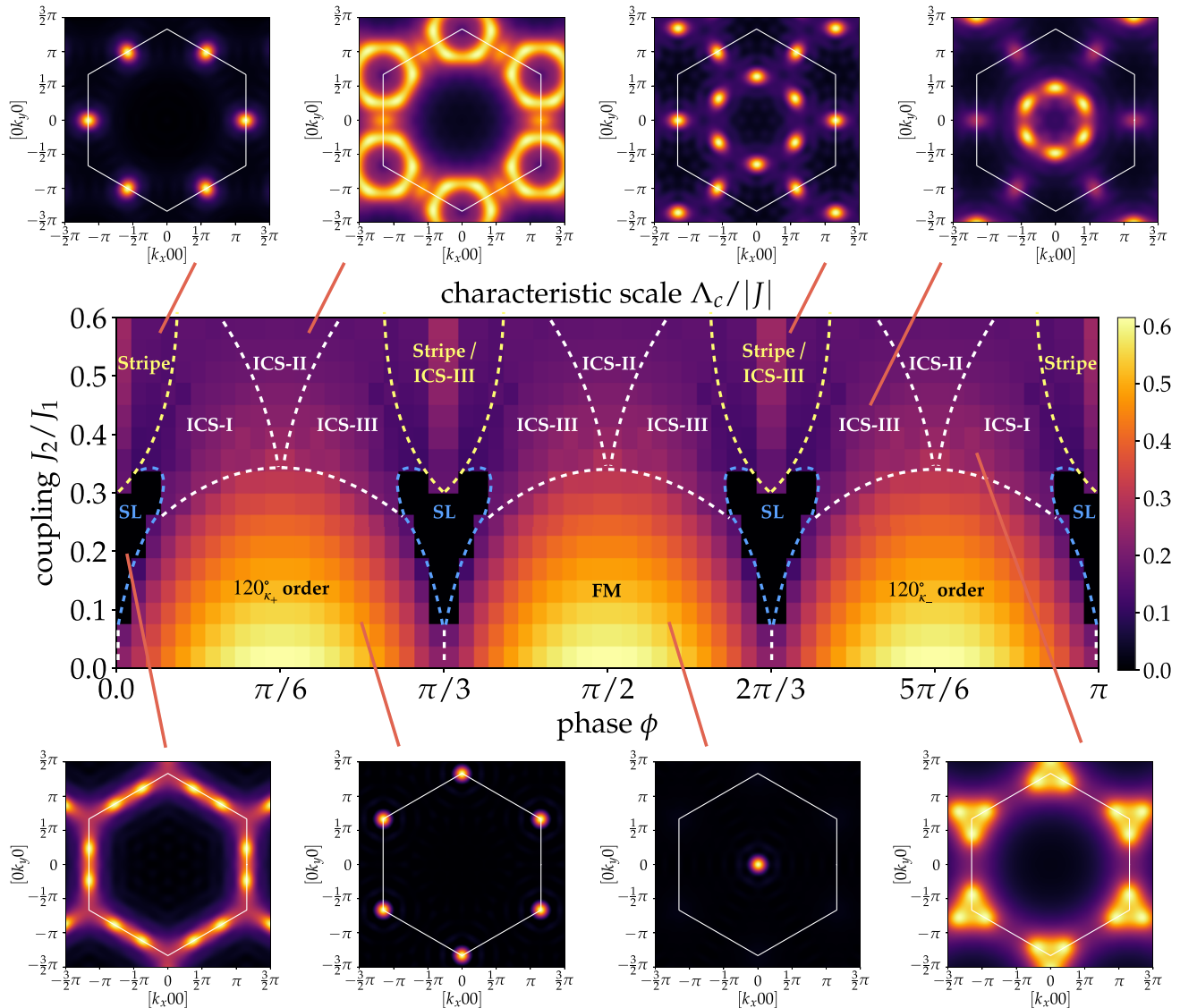

FIG. 1. Magnetic phase diagram for tWeS$_2$ obtained from pf-FRG. We plot the characteristic RG scale Λ_c indicating the emergence of magnetic long-range order or the absence thereof. In total, we identify a plethora of nine potential phases (SL: spin liquid, ICS: incommensurate spin spiral, and FM: ferromagnet), including a putative quantum spin liquid for ϕ close to integer multiples of $\pi/3$ and finite second-nearest neighbor Heisenberg coupling J_2/J_1. The surrounding heat maps display the full elastic component of the structure factor [i.e., $\sum_\mu \chi_{\mu\mu}^{\Lambda_c}(\mathbf{k}, iw = 0)$], measurable, for example, by neutron scattering experiments. Further details about the different phases and how they are identified in our numerical calculations can be found in Secs. III A, III B 1, and III C of the main text.

In this article, we set out to study the effective spin model proposed for tWSe$_2$,[44,45] augmented by an antiferromagnetic second-nearest neighbor Heisenberg coupling J_2 previously not considered, using both classical *and* quantum many-body methods. In the classical limit, we first use the Luttinger–Tisza (LT) method to determine the likely magnetic orders at zero temperature. We then investigate their stability with respect to thermal fluctuations and a strictly enforced constraint on the length of the classical $O(3)$ spins by performing classical Monte Carlo (MC) simulations. The quantum phase diagram is mapped out utilizing state-of-the-art pseudo-fermion functional renormalization group (pf-FRG) calculations and (infinite) density matrix renormalization group[51–53] techniques (iDMRG).

Our key results are summarized in Fig. 1. In order to discuss them in a concise manner, we first focus on the regime $\phi \in \left[0, \frac{\pi}{6}\right]$ as the remainder of the phase diagram can be related via a simple three-sublattice mapping (see Sec. II). The three main features of this regime can then be phrased in the following way: (1) Both classically and quantum mechanically, we find that the 120° order, featuring, for $\phi > 0$, a finite vector chirality κ (discussed in the following), becomes more stable with increasing ϕ. (2) At large J_2, finite ϕ tends to favor one of the two incommensurate spin spiral states over the stripe order expected for the pure J_1–J_2 model. Classically, any finite ϕ suffices to generate incommensurate correlations, whereas quantum mechanically, the stripe order seems to remain stable for small ϕ. (3) Close to the Heisenberg limit, a paramagnetic region is identified for finite values of J_2, indicating a putative realm for quantum spin liquid (QSL) physics. This regime, however, quickly diminishes with increasing ϕ. These observations can straightforwardly be generalized to the parameter space beyond $\phi = \pi/6$, albeit with new labels for the different phases. For example, close to $\phi = \pi/3$, one finds a ferromagnetic (FM) ground state instead of the chiral 120° orders found at $\phi = 0$ and $\phi = 2\pi/3$.

The remainder of this article is structured as follows: First, following the arguments of previous microscopic considerations,[44] the derivation of the effective tWSe$_2$ spin model, starting from the corresponding tight-binding Hamiltonian, is recapped. We then summarize known results for the $J_2 = 0$ limit and elaborate on symmetry properties of the strong coupling Hamiltonian. Second, the results obtained within the Luttinger–Tisza method and classical Monte Carlo simulations are discussed. Next, we introduce the pf-FRG and iDMRG methods and present their implications for the quantum phase diagram. We conclude by evaluating the relevance of our results for future experimental studies of tWSe$_2$ and pointing out further possible research directions.

II. MODEL

We focus on homobilayers of tWSe$_2$, which have recently been studied both experimentally,[31,54] using transport and scanning tunneling microscopy (STM) measurements, as well as theoretically,[31,44,45] using mean-field approaches. The STM measurements have demonstrated that the moiré valence bands originate from the $\pm K$ valleys of the two TMD layers, while the Γ valley is energetically disfavored. Spin degrees of freedom are thereby locked to one of the two valleys, giving rise to an effective spin–orbit coupling in the corresponding tight-binding Hamiltonian on the triangular superlattice,[44,45]

$$H_t = \sum_{\alpha \in \{\uparrow,\downarrow\}} \sum_{\langle ij \rangle} t_{ij}^\alpha c_{i\alpha}^\dagger c_{j\alpha}^\dagger + \text{h.c.}, \qquad (1)$$

which is a valid description of tWSe$_2$ for small commensurate twist angles $\theta \gtrsim 3°$, where lattice relaxation effects and further neighbor hoppings can be neglected.[44] Note that because of the aforementioned spin-valley locking, the sum over spin degrees of freedom α should be a understood as a simultaneous sum over valleys.

Due to time-reversal and point group symmetries, the hoppings t_{ij}^α have to obey $t_{ij}^\alpha = \bar{t}_{ji}^\alpha$ and $t_{ij}^\alpha = \bar{t}_{ij}^{\bar\alpha}$, while also being invariant under only threefold lattice rotations.[44] More specifically, the dispersion for the tight-binding Hamiltonian in Eq. (1) reads

$$\varepsilon_\alpha(\boldsymbol{k}) = -2|t| \sum_{\boldsymbol{\delta}_{nn}} \cos(\boldsymbol{k}\boldsymbol{\delta}_{nn} + \alpha\phi) \qquad (2)$$

with $|t| = |t_{\langle ij \rangle}^\alpha| \sim 1$ meV defining the energy scale of the model.[44] Here, $\boldsymbol{\delta}_{nn}$ sums over three out of six nearest neighbor displacement vectors of the triangular lattice with an equal phase ϕ (see Fig. 2). Density functional theory (DFT) calculations imply that the latter can be varied between $\pm\pi/3$ by an out-of-plane displacement field $|V_z| \lesssim 100$ meV, which shifts the energies at the K and K' points of the mini-Brillouin zone in opposite directions and thus breaks the approximate inversion symmetry of the bilayer system.[31,44,45] A spin–orbit coupled generalized Hubbard model results by combining the tight-binding Hamiltonian (1) with an on–site interaction U. This on–site interaction has been found to be about one order of magnitude larger than the kinetic contribution,[44] motivating a strong coupling description.
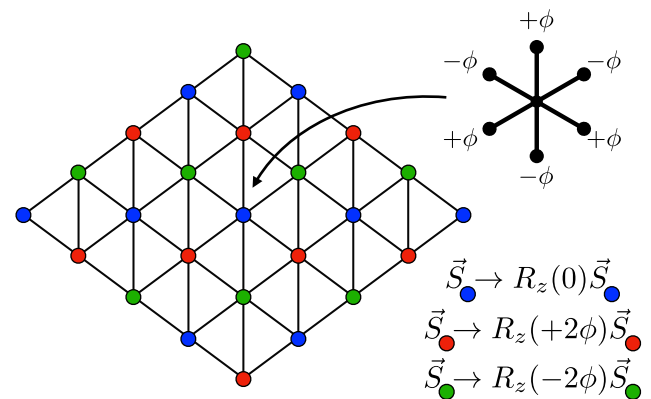

FIG. 2. Three-sublattice rotation for the triangular lattice model. The anisotropic phase ϕ_{ij} changes sign between nearest neighbor bonds (as shown in the upper right corner). The Hamiltonian (3) can be recast in terms of out-of-plane rotation matrices $R_z(-2\phi_{ij})$ [see Eq. (4)]. By rotating the spins on the three sublattices (see the lower right corner), each nearest neighbor term in Eq. (4) can be transformed into an SU(2) symmetric Heisenberg interaction, except for terms coupling the red and green sublattices. The remaining rotation, by -6ϕ, vanishes for $\phi = n\frac{\pi}{3}$ with $n \in \mathbb{Z}$.

In this work, we consider the $U \gg |t|$ limit at half-filling, where one can derive an effective spin model[44,45] with residual U(1) symmetry about the z axis,

$$H = J_1 \sum_{\langle ij \rangle} \left[\cos(2\phi_{ij})(S_i^x S_j^x + S_i^y S_j^y) + S_i^z S_j^z \right]$$
$$+ J_1 \sum_{\langle ij \rangle} \sin(2\phi_{ij}) \, \hat{z} \cdot (\mathbf{S}_i \times \mathbf{S}_j) + J_2 \sum_{\langle\langle ij \rangle\rangle} \mathbf{S}_i \cdot \mathbf{S}_j, \quad (3)$$

featuring XXZ, off-diagonal Dzyaloshinskii–Moriya (DM) and SU(2) symmetric next-nearest neighbor Heisenberg interactions. The phase ϕ_{ij} varies sign between nearest neighbor bonds (see Fig. 2), thus inheriting the reduction from sixfold to threefold lattice rotational symmetry from the tight-binding model (1). As pointed out in Ref. 44, the form of the underlying second-nearest neighbor hopping motivates the inclusion of a fully SU(2) symmetric Heisenberg interaction J_2, which has previously not been considered. For large displacement fields $|V_z| > 50$ meV, this J_2 is the next largest interaction beyond the nearest neighbor J_1 terms (with $J_1 \sim 1$ meV).[44]

For $J_2 = 0$, the ground state phase diagram of Eq. (3) has previously been studied using classical Luttinger–Tisza and self-consistent Hartree–Fock mean-field calculations.[44,45] For $\phi \in [0, \pi]$, both works find a ferromagnetic phase ($\pi/3 < \phi < 2\pi/3$) sandwiched between two antiferromagnetic 120° orders with opposite vector chiralities $\kappa_\pm$ with $\kappa = \text{sgn}(\hat{z} \cdot (\mathbf{S}_1 \times \mathbf{S}_2 + \mathbf{S}_2 \times \mathbf{S}_3 + \mathbf{S}_3 \times \mathbf{S}_2))$, where $\mathbf{S}_1, \mathbf{S}_2$, and $\mathbf{S}_3$ are spins on a triangular plaquette. For finite J_2, however, the situation has not yet been studied and quantum fluctuations could stabilize more exotic phases especially since the several numerical works[46–50] suggest that the pure J_1–J_2 Heisenberg model on the triangular lattice hosts a quantum spin liquid ground state.

For finite $\phi = n\frac{\pi}{3}$ with $n \in \mathbb{Z}$, the nearest neighbor terms can be transformed into a fully SU(2) symmetric form by performing a three-sublattice rotation (see Fig. 2), thus opening up the possibility to experimentally tune the system close to the (effective) Heisenberg limit by variation of the displacement field.[44,45] This can be clearly seen by rewriting the Hamiltonian as

$$H = J_1 \sum_{\langle ij \rangle} \mathbf{S}_i^{\text{T}} R_z(-2\phi_{ij}) \mathbf{S}_j + J_2 \sum_{\langle\langle ij \rangle\rangle} \mathbf{S}_i \cdot \mathbf{S}_j, \quad (4)$$

where $R_z(-2\phi_{ij})$ is an out-of-plane rotation matrix with rotation angle $-2\phi_{ij}$ and then performing the transformation shown in Fig. 2. Indeed, more generally, the energetics at ϕ, $\phi + n\pi/3$, and $n\pi/3 - \phi$ are identical although crucially the wavefunctions do change.

With these observations in mind, we therefore focus our efforts on the regime $\phi \in [0, \frac{\pi}{6}]$ and study the respective ground states by classical Luttinger–Tisza and Monte Carlo simulations as well as quantum pf-FRG and iDMRG calculations that go beyond mean-field theory. The global phase diagram can then be straightforwardly obtained using the sublattice rotation outlined above and adjusting the labels of the phases accordingly.

III. RESULTS

A. Classical limit

First, we explore the classical $S \to \infty$ limit of the model. In order to determine the likely classical magnetic orders, we turn to the Luttinger–Tisza (LT) method.[55] This method treats the spin as an unconstrained vector, allowing for a straightforward Fourier transform and subsequent diagonalization of any quadratic spin Hamiltonian. For the model in Eq. (3), the corresponding energy eigenvalues are

$$E_H(\mathbf{k}) = J_1 \sum_{\boldsymbol{\delta}_1} \cos(\mathbf{k} \cdot \boldsymbol{\delta}_1) + J_2 \sum_{\boldsymbol{\delta}_2} \cos(\mathbf{k} \cdot \boldsymbol{\delta}_2),$$
$$E_\pm(\mathbf{k}) = J_1 \sum_{\boldsymbol{\delta}_1} \cos(\mathbf{k} \cdot \boldsymbol{\delta}_1 \pm 2\phi_{ij}) + J_2 \sum_{\boldsymbol{\delta}_2} \cos(\mathbf{k} \cdot \boldsymbol{\delta}_2), \quad (5)$$

where $\boldsymbol{\delta}_1$ and $\boldsymbol{\delta}_2$ are the set of nearest and next-nearest neighbor lattice vectors. $E_H(\mathbf{k})$ is independent of ϕ and is identical to the Heisenberg result (i.e., $\phi = 0$) with the eigenvalue lying purely along the z axis. On the other hand, $E_\pm(\mathbf{k})$ are explicitly ϕ dependent with eigenvalues lying purely within the xy-plane. For a given set of parameters, the absolute minimum eigenvalue provides a strict lower bound to the classical energy, and the corresponding momenta, which we denote by $\mathbf{k}^\star$, provide candidate classical ordering wavevectors. They also provide crucial clues as to what correlations one might expect in the quantum case, where the spins are not subject to a hard classical constraint.

For $\phi = 0$, i.e., the J_1–J_2 Heisenberg model, there is a transition from 120° order with ordering wavevector $\mathbf{k}^\star = K$ to stripe order with $\mathbf{k}^\star = M$ at a critical value of $J_2/J_1 = 1/8$. Turning on a small finite $\phi \neq 0$ has three important consequences: (i) it forces the spins to order within the xy-plane [$E_\pm(\mathbf{k})$ are always favored], (ii) it selects a definite chirality and helps stabilize the 120° order, increasing its extent to a maximum of $J_2/J_1 = 1/3$ at $\phi = \pi/6$, and (iii) it immediately turns the stripe order incommensurate, which we label ICS-I, with ordering wavevectors $\mathbf{k}^\star$ that lie along the high-symmetry $M - K$ line (and $M - K'$ line although from here on we will simply use K when no further distinction is necessary). It also generates a new ordered phase, clustered close to $\phi = \pi/6$, with incommensurate magnetic order and associated ordering wavevectors that do not lie on any high-symmetry line, which we label ICS-II. Note that due to the low-symmetry when $\phi \neq 0$, the Luttinger–Tisza method does not support classical coplanar spirals with just a single $\mathbf{k}^\star$,[56] meaning that the ICS phases must be multi-$\mathbf{k}$ spirals (see the supplementary material for further information).

As noted in Sec. II, the physics of the model for $\phi > \pi/6$ can be related to the region $\phi \in [0, \frac{\pi}{6}]$ discussed above via a simple three-sublattice transformation. Indeed, this can also be seen from the form of the LT eigenvalues with $E_\pm(\mathbf{k}) \to E_\pm(\mathbf{k} \pm n\mathbf{K})$ for $\phi \to \phi + n\pi/3$. Thus, the 120° order gets mapped to FM order, and the ICS-I phase with $\mathbf{k}^\star$ along the $M - K$ line gets mapped to a new ICS-III phase with $\mathbf{k}^\star$ along the $K - \Gamma$ line. All phases remain ordered within the xy-plane. The classical Luttinger–Tisza phase diagram is summarized in Fig. 3(a).

Classical Monte Carlo (MC) simulations allow us to explore the relative stability of the different phases as well as to confirm that the
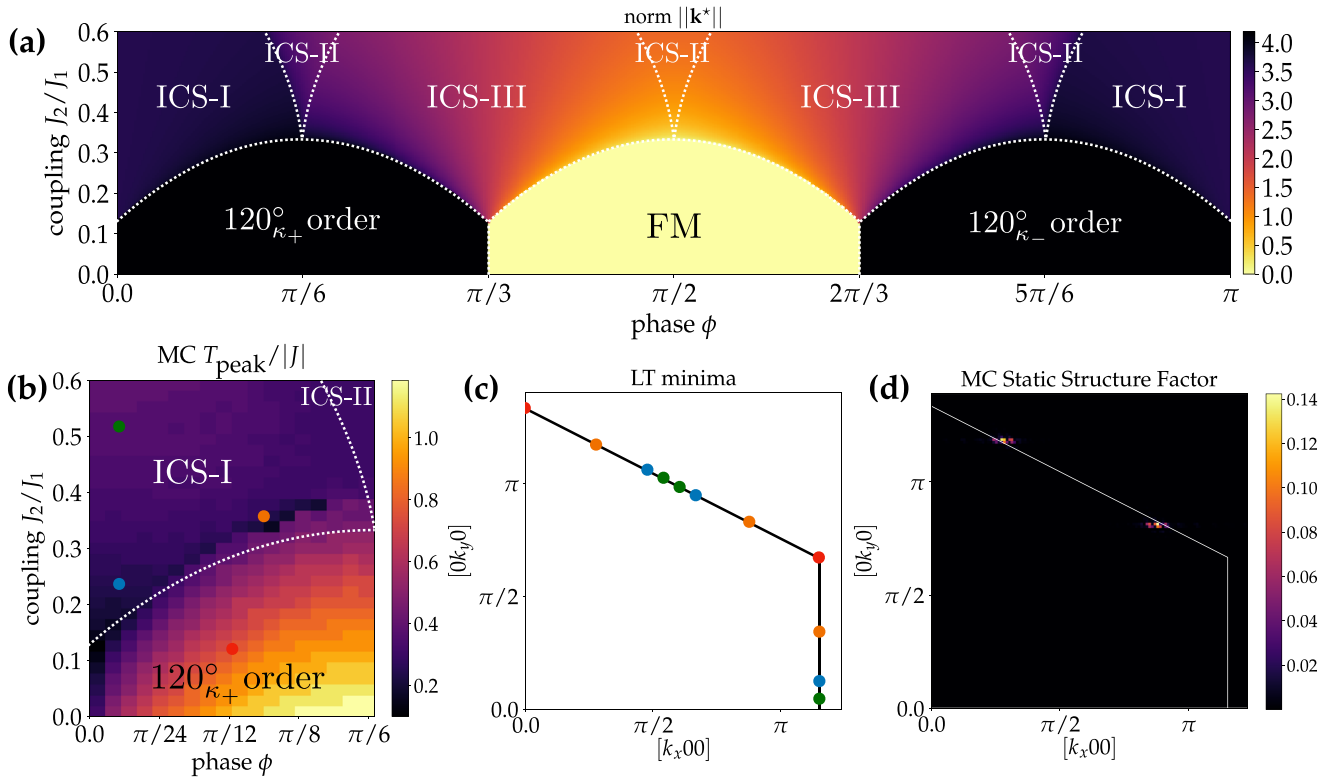
FIG. 3. Classical phase diagram with (a) the Luttinger–Tisza (LT) result. Six distinct phases are visible, a simple ferromagnetic order (FM), two 120° orders with vector chirality κ_+ and κ_-, and three incommensurate phases, ICS-I, ICS-II, and ICS-III. The background color indicates the norm of the ordering wavevector $\|\mathbf{k}^\star\|$. (b) Classical Monte Carlo results on a 96×96 lattice for the peak temperature T_{peak} from the specific heat across the phase diagram with the LT phase boundaries overlaid on top. (c) Locations of the LT ordering wavevectors $\mathbf{k}^\star$ for the four points marked in (b) with, for example, the green dots in (c) marking the LT ordering wavevectors for the green parameter point in (b) (see Fig. 4 for the spin-1/2 pf-FRG structure factors at the same points). (d) Classical static spin structure factor at low temperature obtained by Monte Carlo simulations at the point $J_2/J_1 = 0.36$ and $\phi = \pi/10$ [orange point in (b) and (c)] within the ICS-I phase. The two sharp peaks lie at the same incommensurate momenta as the LT minima shown in (c).

Luttinger–Tisza $\mathbf{k}^\star$ are correct. As the model contains a continuous U(1) rotational symmetry about the z axis, the Mermin–Wagner theorem precludes a finite in-plane magnetization at finite temperature. However, a peak in specific heat at T_{peak} related to a Berezinskii–Kosterlitz–Thouless (BKT) transition due to ordering in the xy-plane is still possible,[57,78] as seen, for example, in the triangular lattice XXZ model [the first term in Eq. (3)].[58] A map of T_{peak} is shown in Fig. 3(b) with, as expected, the highest T_{peak} ~ $1.5J_1$ occurring for $J_2/J_1 = 0$ and $\phi = \pi/6$, a consequence of the enhanced stability for the 120° order that finite ϕ provides. On the other hand, within the incommensurate phases, T_{peak} shows little variation, lying between 0.4 and $0.5J_1$ for the whole range shown. Finally, Fig. 3(d) shows an example of the static spin structure factor taken from the MC within the ICS-I phase. There are two peaks at incommensurate wavevectors located along the $M - K$ and $M - K'$ high-symmetry lines whose location precisely matches two of the ordering wavevectors $\mathbf{k}^\star$ predicted by the Luttinger–Tisza method [the orange dots in Fig. 3(c)]. This is accompanied by a complex real space structure (see the supplementary material for examples).

B. Pseudo-fermion functional renormalization group

1. Method

In the past decade, the pseudo-fermion functional renormalization group (pf-FRG) developed by Reuther and Wölfle[59] has been widely employed to investigate ground state phase diagrams of quantum spin models on two[59,60] and three[61] dimensional lattices. The method utilizes the parton decomposition,

$$S_i^\mu = \frac{1}{2} \sum_{\alpha,\beta} f_{i\alpha}^\dagger \sigma_{\alpha\beta}^\mu f_{i\beta}, \tag{6}$$

to recast the original Hamiltonian in terms of fermionic creation and annihilation operators. Here, $\sigma_{\alpha\beta}^\mu$ for $\mu \in \{x, y, z\}$ denote Pauli matrices. Changing the representation space of the spin algebra, however, comes with a caveat: The dimensions of the (local) Hilbert space of pseudo-fermions ($d = 4$) and spin-1/2 operators ($d = 2$) are different, and as such, the respective representations are not isomorphic. Although unphysical states can be eliminated by an additional local constraint $\sum_\alpha f_{i\alpha}^\dagger f_{i\alpha} = 1$ on every lattice site, an exact treatment of

this constraint is rather difficult, and in practice, the softened condition $\langle \sum_\alpha f_{i\alpha}^\dagger f_{i\alpha}^\dagger \rangle = 1$ is employed. Fluctuations around the mean have been found to leave observables computed within pf-FRG qualitatively unchanged,[62,63] advocating an on-average treatment of the fermionic number constraint at zero temperature.

Having rewritten the spin Hamiltonian in terms of fermions, a regulator function, here chosen as

$$\Theta^\Lambda(w) = 1 - e^{-w^2/\Lambda^2} \tag{7}$$

with flow parameter Λ, is implemented in the bare propagator as

$$G_0(w) \rightarrow G_0^\Lambda(w) = \Theta^\Lambda(w) G_0(w). \tag{8}$$

This procedure gives rise to Λ-dependent n-point correlation functions whose flow from the ultraviolet $G_0^{\Lambda\to\infty}(w) = 0$ to the infrared $G_0^{\Lambda\to 0}(w) = G_0(w)$ limit is governed by a hierarchy of ordinary integro-differential flow equations. To be amenable to numerical algorithms, the latter has to be truncated. Here, we utilize the Katanin truncation,[59,62,64] which cuts off the flow equations beyond the two-particle vertex and has been demonstrated to efficiently capture competing magnetic and non-magnetic phases.[65]

The main observable extracted from the pf-FRG is the flowing spin–spin correlation function,

$$\chi_{ij}^{\mu\nu\Lambda}(iw = 0) = \int_0^\beta d\tau \langle T_\tau S_i^\mu(\tau) S_j^\nu(0) \rangle^\Lambda, \tag{9}$$

which shows an instability (such as a cusp, kink, or divergence) once the RG flow selects a ground state with broken symmetries. The absence of such a breakdown is consequently associated with paramagnetic phases such as spin liquids. Furthermore, for long-range ordered states, the respective type of magnetic order can be characterized by Fourier transforming $\chi_{ij}^{\mu\nu\Lambda}$ to momentum space ($F[\chi_{ij}^{\mu\nu\Lambda}](\mathbf{k}) = \chi_{\mu\nu}^\Lambda(\mathbf{k})$) and determining the wavevectors $\mathbf{k}_{max}$ with the largest spectral weight. Further information on the method and its numerical implementation is provided in Sec. I of the supplementary material.

Due to the symmetry properties of Eq. (3), we consider two distinct susceptibilities $\chi_{XX}^\Lambda(\mathbf{k})$ ($= \chi_{YY}^\Lambda(\mathbf{k})$) and $\chi_{ZZ}^\Lambda(\mathbf{k})$ in momentum space to distinguish possible in-plane and out-of-plane magnetic orders. While finite, in general, for $\phi_{ij} > 0$, off-diagonal correlation functions $\chi_{XY}^\Lambda(\mathbf{k})$ ($= -\chi_{YX}^\Lambda(\mathbf{k})$) turn out to be rather small compared to their diagonal counterparts in our pf-FRG calculations and are therefore only considered as a benchmark to check for a switch in vector chirality between the two 120° orders.

2. Phase diagram

We now turn to the discussion of the $\phi \in [0, \frac{\pi}{6}]$ region of the phase diagram of our model Hamiltonian Eq. (3), as obtained within pf-FRG and summarized in Fig. 4.

For small $\phi \lesssim \pi/48$ and intermediate next-nearest neighbor coupling, we find a small region of spin liquid behavior, where the RG flow [see the blue curve in Fig. 4(c)] stays smooth and featureless down to the lowest simulated cutoff value $\Lambda/|J| = 0.05$, where $|J| = \sqrt{J_1^2 + J_2^2}$. For $\phi = 0$, corresponding to the pure J_1–J_2 Heisenberg model, the estimated range of the spin liquid regime $0.12 \lesssim J_2/J_1 \lesssim 0.32$ is larger than the respective literature values 0.06–0.08

$\lesssim J_2/J_1 \lesssim 0.15$–0.17, which we attribute to our softened treatment of the fermionic number constraint and the exclusion of higher loop corrections in the current framework. Since the FRG calculation is nevertheless capable of reproducing the existence of a paramagnetic regime between the adjacent 120° and stripe ordered phases (consistent with previous studies[60]), we are confident that its qualitative predictions of the phase diagram are reliable. The structure factor $\sum_\mu \chi_{\mu\mu}^\Lambda(\mathbf{k})$ within the SL phase is displayed in Fig. 4(d). It resembles an interpolation between the 120° and stripe orders [Figs. 4(e) and 4(f)] in the sense that its peaks move on the high-symmetry line between the K and M points of the first Brillouin zone as J_2 and ϕ are increased. In this regard, the spin liquid region appears similar to a molten version of the neighboring incommensurate spin spiral phase [ICS-I in Figs. 4(a) and 4(b)], albeit with a washed out distribution of the subleading weight along the Brillouin zone edges. The spectral weight for the ICS-I phase is, in contrast, much more localized although, of course, the maxima still reside at incommensurate positions between the K and M points [Fig. 4(g)].

For larger ϕ, we find the pf-FRG phase diagram to be roughly consistent with the classical result (Fig. 3), predicting, for $J_2/J_1 \gtrsim 0.32$, a transition from in-plane 120° order to one of the two incommensurate phases that can be distinctly identified by the position of their ordering wavevector $\mathbf{k}_{max}$ within the first Brillouin zone [Fig. 4(b)]. The phase boundary is, however, shifted upward in favor of the 120° order within the FRG. We generally find the dominant contributions to the structure factor to stem from the in-plane correlations, i.e., $\chi_{XX}^\Lambda + \chi_{YY}^\Lambda$, where flow breakdowns are most visible although out-of-plane correlations become sizable with increasing J_2. This finding is in line with the Luttinger–Tisza result Eq. (5) as the eigenvalues corresponding to in-plane and out-of-plane order move closer together.

Notably, our pf-FRG approach also finds a stripe ordered ground state for $J_2/J_1 \gtrsim 0.32$–0.36 and close to $\phi = 0$. In contrast, our classical calculations predict the stripe order to be unstable to incommensurate ordering for any finite ϕ. This could be, on the one hand, due to finite size effects in the pf-FRG calculations (although for increased lattice truncation ranges, no changes are observed), which would make it difficult to decipher the extremely weak classical incommensuration at small ϕ. On the other hand, quantum fluctuations may also favor the commensurate stripe order over the ICS-I phase especially since their classical energies for small ϕ and large J_2 are almost degenerate. We also note that the signatures for magnetic ordering as characterized by a breakdown of the RG flow [see Fig. 4(c)] are rather weak in the incommensurate phases (pronounced shoulder vs sharp peak or divergence in the stripe and 120° phase), hinting toward strongly competing magnetic and non-magnetic channels within the FRG approach for this part of the phase diagram.

For $\phi > \pi/6$, as before, the structure of the model outlined in Sec. II allows us to straightforwardly generalize our results (see Fig. 1), while adjusting the labels for the different phases. For $\pi/3 < \phi < 2\pi/3$, antiferromagnetic 120° order is replaced by a ferromagnetic ground state, which yet again becomes 120° ordered although with opposite vector chirality for $2\pi/3 < \phi < \pi$. At large J_2 and $\pi/6 < \phi < 5\pi/6$, the ICS-I order gets mapped to another incommensurate spin spiral phase (ICS-III) with susceptibility maxima located on the high-symmetry line between the Γ and K points. Finally, the stripe order found close to the Heisenberg limit $\phi = 0$ re-appears
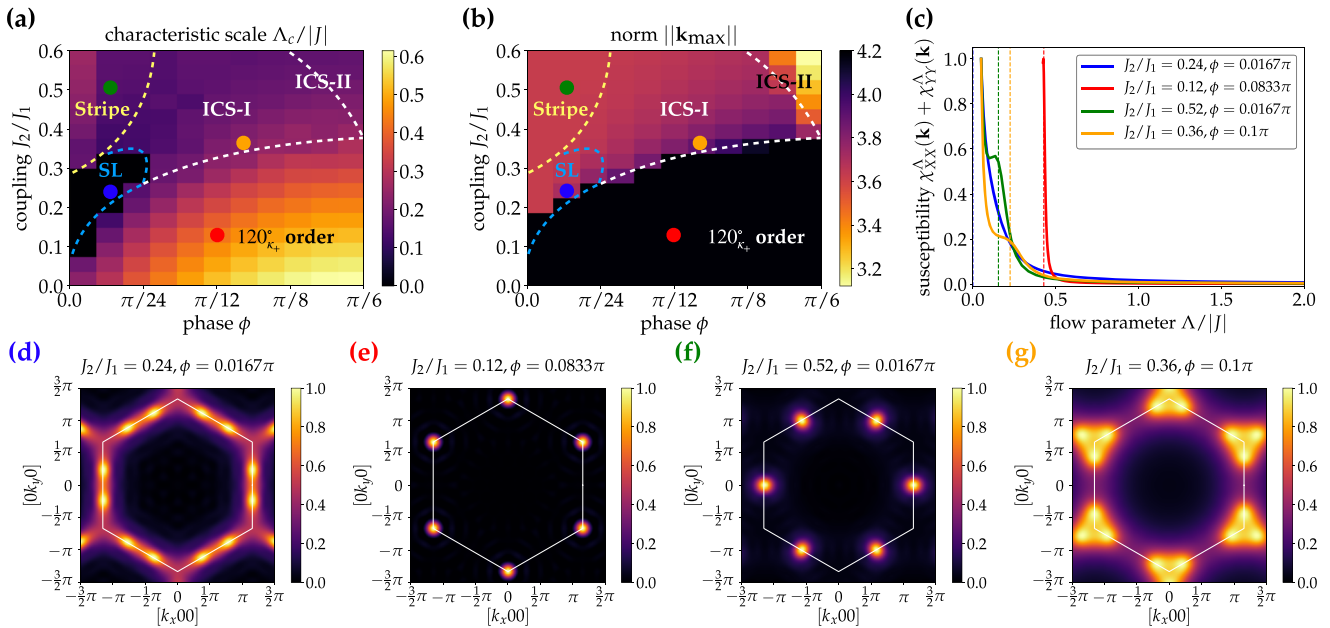
FIG. 4. Phase diagram for $\phi \in \left[0, \frac{\pi}{6}\right]$ obtained from pf-FRG. In (a), the characteristic RG scale Λ_c is shown as a function of antiferromagnetic next-nearest neighbor coupling J_2/J_1 and phase $0 \le \phi \le \pi/6$ with approximate phase boundaries drawn as a guide to the eye. We find a small region of quantum spin liquid (SL) behavior for small $\phi < \pi/24$ and intermediate values of $0.12 < J_2/J_1 < 0.32$, where the RG flow [see the blue curve in panel (c)] stays smooth and featureless down to the lowest accessible cutoff values. The rest of the phase diagram is occupied by four different magnetically ordered phases, which can be distinguished by their ordering wavevector $\mathbf{k}_{max}$ and its respective norm, as displayed in (b). For the stripe and 120° ordered phases (with definite vector chirality κ_+), $\mathbf{k}_{max}$ resides at the M and K points, respectively, whereas it continuously changes the position in the spin liquid and incommensurate spin spiral (ICS) phases, as apparent from the color gradient in (b). In (c), we show representative flows of the magnetic susceptibility as a function of the RG scale $\Lambda/|J|$ with dashed lines highlighting the position of the characteristic scale $\Lambda_c/|J|$ (which is most visible for the in-plane correlators). The latter can be distinctly identified for the stripe and 120° phase, whereas the incommensurate phases only show a pronounced shoulder, indicating strongly competing tendencies between magnetic and non-magnetic channels in the pf-FRG equations. The flows have been normalized by their respective maximum for better comparability. Finally, (d)–(g) display the full, diagonal structure factors $\sum_\mu \chi_{\mu\mu}^\Lambda(\mathbf{k})$ computed at the characteristic scale Λ_c for the four points marked with colored dots in (a) and (b).

close to $\phi = \pi/3$ and $\phi = 2\pi/3$ in coexistence with the ICS-III order (see Fig. 1 in the supplementary material for further details).

C. Density matrix renormalization group

To complement our numerical results, we now present our iDMRG calculations of the model for two representative J_2 cuts at $\phi = \pi/48$ and $\pi/12$ on an infinite cylinder geometry. We use the two-site iDMRG algorithm[51,52] to optimize infinite matrix product states (iMPSs) as approximations to the ground state wavefunctions. We chose the bond dimension such that the error is smaller than the marker size in every plot.[66] The two-site iDMRG truncation errors are at most of the order of 10^{-7}.

The cylinder geometry is illustrated in Fig. 5(a). We choose a circumference $L_y = 6$, compatible with the possible 120° and stripe orders, with an example of the latter shown in the same inset. The infinite cylinder geometry then allows us to probe possible incommensurate correlations along the infinite direction.

Recall that finite ϕ explicitly breaks SU(2) symmetry down to a residual in-plane U(1) symmetry. According to the Mermin–Wagner theorem for quasi-one-dimensional systems (such as our cylindrical iDMRG geometry), an in-plane 120° order

that spontaneously breaks U(1) symmetry is forbidden. However, the existence of a possible two-dimensional 120° phase can be inferred by studying spin–spin correlations. On the other hand, long-range out-of-plane stripe order does not break any continuous symmetry and can therefore be directly observed within our iDMRG calculations.

We study the out-of-plane, $\langle S_0^z S_{n\mathbf{a}_2}^z \rangle$, and in-plane, $\langle S_0^+ S_{n\mathbf{a}_2}^- \rangle$, spin–spin correlation functions, where $\mathbf{a}_2$ is the lattice vector along the infinite direction [see Fig. 5(a)] and $S_i^\pm = S_i^x \pm iS_i^y$. Using the iMPS data, it is known that static correlation functions of this form can be written as $\sum_j C_j e^{ik_j n} e^{-n/\xi_j}$,[53] where j sums over eigenvectors of the iMPS transfer matrix. The largest ξ_j corresponds to the dominant correlation length, while the respective k_j then characterizes the momentum of the lowest-lying excitation along the infinite direction. The correlation length spectrum has, for example, been used to study the $\phi = 0$ case in Ref. 47.

Within the correlation length spectrum, the 120° order for the SU(2) symmetric case corresponds to a dominant correlation length at $k = \pm 2\pi/3$, equal in magnitude for both in- and out-of-plane components. For finite ϕ, however, our classical and pf-FRG calculations indicate that 120° order is not only locked to the xy-plane but
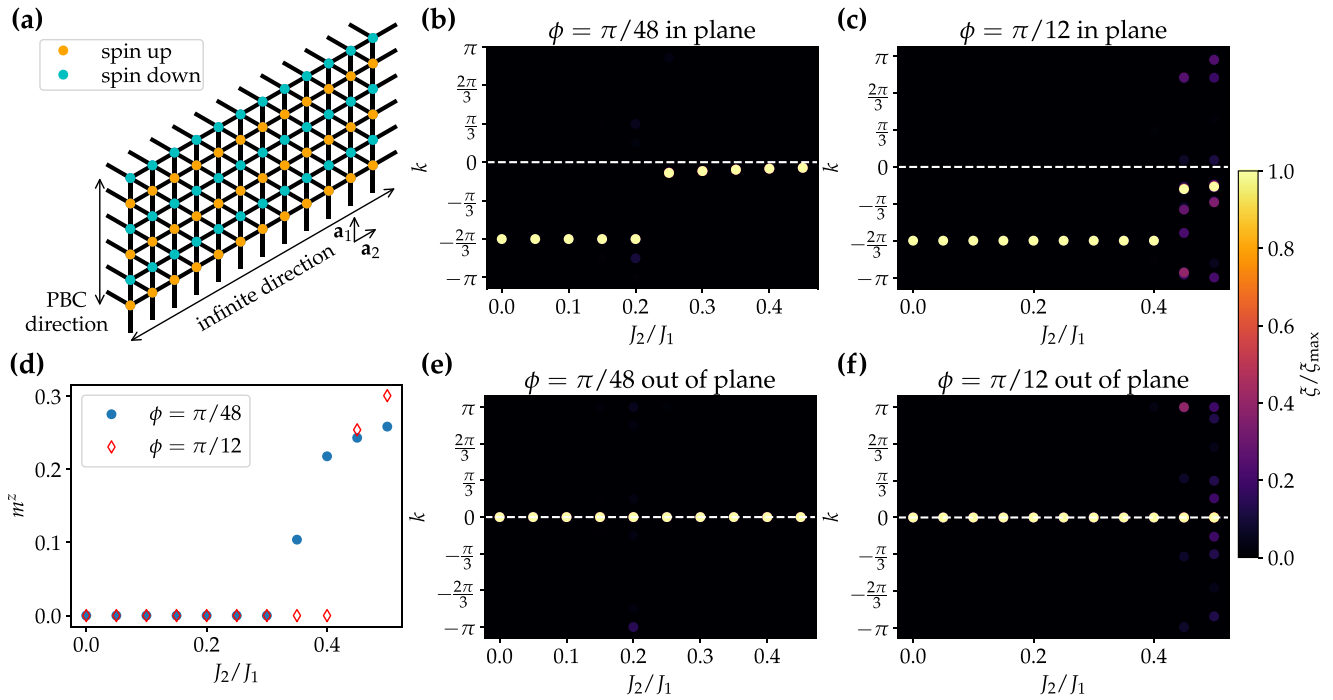
FIG. 5. Correlation length spectrum on an infinite cylinder geometry. (a) shows the triangular lattice on an infinite cylinder geometry with an $L_y = 6$ site circumference. A configuration of the possible out-of-plane stripe order is illustrated by the coloring of sites in orange (cyan), indicating an out-of-plane spin up (down). (b)–(f) show the correlation length spectra (see the main text for definition) along the infinite direction for $\phi = \pi/48$ and $\pi/12$. For each value of J_2/J_1, we plot the 20 largest correlation lengths at their respective k values. For most cases, few points are visible as they share the same k. Finally, in (d), the out-of-plane staggered magnetization along the cylinder direction, m^z, is plotted. The evidence for the in-plane 120° phase is the dominant in-plane correlation length at $-2\pi/3$. In-plane incommensurate correlations are visible for relatively large J_2 in both (b) and (c), where the momenta are not locked to high-symmetry points, but are instead distributed around $-\pi/10$ and $-\pi/6$, respectively. The indication for out-of-plane stripe order is given by a non-vanishing m^z in (d).

also locked to a certain chirality. Our DMRG data (see Fig. 5) are consistent with these results as we observe that only in-plane correlations display a peak at $k = -2\pi/3$.

For large J_2 and $\phi \neq 0$, we find incommensurate correlations characterized by a continuously varying momentum in Figs. 5(b) and 5(c). Curiously, the incommensurate correlations can exist either with or without an accompanying finite out-of-plane staggered magnetization along the cylinder direction, $m^z = \sum_y |\langle S_y^z e^{i\pi y} \rangle|/L_y$.[79] For the chosen cylinder geometry, an out-of-plane stripe order with stripes parallel to the infinite $\mathbf{a}_2$ direction [shown in Fig. 5(a)] has a finite m^z. For $\phi = \pi/48$, we observe a relatively large region, $0.2 \lesssim J_2/J_1 \lesssim 0.3$, with in-plane incommensurate correlations and with negligible out-of-plane components, $S_i^z \approx 0$. This is consistent with the pf-FRG structure factor computed in the putative spin liquid phase, Fig. 4(d), where residual but broadened incommensurate peaks are visible. On the other hand, for larger J_2, we obtain a finite out-of-plane m^z [see Fig. 5(d)], consistent with the onset of out-of-plane stripe order. For $\phi = \pi/12$, we observe, however, at least within our resolution, just a single direct transition from in-plane 120° order to out-of-plane stripe order, not inconsistent with the absence of a spin liquid in the pf-FRG calculations.

Note, however, that at $\phi = \pi/12$, the pf-FRG predicts that out-of-plane stripe order is much weaker compared to the in-plane

incommensurate correlations [see Fig. 4(e), where peaks at the M point, coming from the out-of-plane component of the structure factor, are overshadowed by the in-plane incommensurate peaks]. The stripe order that we identify in iDMRG may be a finite size artifact of the quasi-one-dimensional cylinder geometry with the possibility that stripe order is molten in favor of the incommensurate in-plane order when going to two dimensions. As the incommensurate correlations are frustrated along the finite direction of the cylinder, the finite size effects should, in fact, be rather large. Our iDMRG calculations may, in turn, be biased toward commensurate stripe order, as opposed to an incommensurate phase. Further simulations with larger L_y, beyond the scope of this work, are necessary to settle on a final conclusion regarding this issue.

IV. DISCUSSION

Twisted TMDs have been predicted to provide an exciting opportunity to realize the physics of the triangular lattice Hubbard model and potentially access the magnetism of its strong coupling limit. By focusing on the particular case of tWSe$_2$ and including both first- and second-nearest neighbor couplings as well as a finite displacement field, we have mapped out the strong coupling phase diagram. Perhaps the most intriguing phase, the QSL that appears

in the pure J_1–J_2 limit, unfortunately only inhabits a small portion of the larger phase diagram, which includes XXZ anisotropy and an effective DM interaction. Accessing QSL physics thus requires tuning the displacement field such that $\phi \sim n\pi/3$ and the twist angle such that J_2/J_1 is within the required range. It is an open question whether further interactions, generated by taking into account further hoppings t_{ij}^α and interactions U_{ij} of the underlying Hubbard model, can lead to a wider, more stable QSL window.

A large part of the phase diagram, above a sufficiently large $J_2/J_1 \sim 0.3$, hosts incommensurate magnetic phases. Such phases can be expected to host gapless phason modes due to the low-energy cost of translating the incommensurate magnetic structure. This is on top of the underlying moiré structure, which, at the atomic level, is generically incommensurate. If it is possible to tune to such a large J_2/J_1 ratio, it would allow to explore the interplay between the moiré scale incommensurate magnetic structure and its gapless phason modes with the atomic scale incommensurate lattice structure and its gapless phonon modes.[67,68]

For smaller ratios of $J_2/J_1 \lesssim 0.3$, the 120° order is stabilized. For $\phi = \pi/6$, it is particularly stable and has a fixed chirality, which leaves only a single BKT transition at finite temperature, with an expected $T_{BKT} \gtrsim J_1$. It thus provides a particularly clean example of BKT physics within potential experimental reach and the possibility of exploring moiré scale magnetic vortices.

An important additional tuning parameter to consider in the future is an external magnetic field. Its effects on the 120° order and J_1–J_2 QSL are already known,[69,70] but how it will distort the incommensurate phases found at finite ϕ is not immediately clear. An interesting possibility would be the formation of multi-Q states. Indeed, such a possibility is actually realized for incommensurate phases found within the pure J_1–J_2 Heisenberg model.[71] In that case, it is even possible to stabilize a skyrmion lattice phase at finite temperature. Realizing a similar scenario for the model at hand with incommensurate phases ICS-I, II, and III would open up a path to studying moiré scale skyrmion lattices within tWSe$_2$.[72]

The phase diagram uncovered in this work expands our view on the landscape of opportunities arising within tTMDs. In particular, the strong coupling physics of tWSe$_2$ has the potential to realize and tune between QSLs, incommensurate magnetic orders, and extremely stable, chiral 120° and ferromagnetic orders. Adding QSL states and incommensurate magnetic orders to the catalog of moiré-controllable phases of matter is an exciting open experimental question, which might be in reach using highly tunable TMDs. We note that the case of tWSe$_2$ was taken here as a prominent experimentally characterized homobilayer example, but the available range of TMDs might help to fabricate other twisted van der Waals materials. In those, e.g., the QSL state could take a more prominent stage in the respective phase diagram.

Note added in proof. During the completion of this article, we became aware of the publication of related (but previously inaccessible) work by Zare and Mosadeq.[73] In contrast to our study, they focus on a honeycomb lattice model, rather than a triangular lattice model, which is then analyzed using the Luttinger–Tisza method (combined with a variational approach to optimize the classical ground states) and DMRG simulations. They find similar conclusions regarding the fate of the quantum spin liquid phases and the stability of magnetic orders.

SUPPLEMENTARY MATERIAL

In addition to the results presented in the main text, further analysis can be found in the supplementary material. This includes a discussion of the real space spin configurations obtained from the classical Monte Carlo simulations, the full trajectory of Luttinger–Tisza wavevectors within the first Brillouin zone upon variation of ϕ, and details on the pf-FRG implementation.

AUTHOR DECLARATIONS

Conflict of Interest

We have no conflicts of interest.

DATA AVAILABILITY

The data that support the findings of this study are available from the corresponding author upon reasonable request.

REFERENCES

[1] Y. Cao, V. Fatemi, A. Demir, S. Fang, S. L. Tomarken, J. Y. Luo, J. D. Sanchez-Yamagishi, K. Watanabe, T. Taniguchi, E. Kaxiras *et al.*, "Correlated insulator behaviour at half-filling in magic-angle graphene superlattices," Nature **556**, 80–84 (2018).

[2] Y. Cao, V. Fatemi, S. Fang, K. Watanabe, T. Taniguchi, E. Kaxiras, and P. Jarillo-Herrero, "Unconventional superconductivity in magic-angle graphene superlattices," Nature **556**, 43–50 (2018).

[3] G. Chen, A. L. Sharpe, E. J. Fox, Y.-H. Zhang, S. Wang, L. Jiang, B. Lyu, H. Li, K. Watanabe, T. Taniguchi *et al.*, "Tunable correlated Chern insulator and ferromagnetism in a moiré superlattice," Nature **579**, 56–61 (2020).

[4] X. Liu, Z. Hao, E. Khalaf, J. Y. Lee, Y. Ronen, H. Yoo, D. Haei Najafabadi, K. Watanabe, T. Taniguchi, A. Vishwanath *et al.*, "Tunable spin-polarized correlated states in twisted double bilayer graphene," Nature **583**, 221–225 (2020).

[5] D. M. Kennes, M. Claassen, L. Xian, A. Georges, A. J. Millis, J. Hone, C. R. Dean, D. N. Basov, A. N. Pasupathy, and A. Rubio, "Moiré heterostructures as a condensed-matter quantum simulator," Nat. Phys. **17**, 155–163 (2021).

[6] H. Yoo, R. Engelke, S. Carr, S. Fang, K. Zhang, P. Cazeaux, S. H. Sung, R. Hovden, A. W. Tsen, T. Taniguchi, K. Watanabe, G.-C. Yi, M. Kim, M. Luskin, E. B. Tadmor, E. Kaxiras, and P. Kim, "Atomic and electronic reconstruction at the van der Waals interface in twisted bilayer graphene," Nat. Mater. **18**, 448–453 (2019).

[7]L. Balents, C. R. Dean, D. K. Efetov, and A. F. Young, "Superconductivity and strong correlations in moiré flat bands," Nat. Phys. **16**, 725–733 (2020).

[8]G. Chen, A. L. Sharpe, P. Gallagher, I. T. Rosen, E. J. Fox, L. Jiang, B. Lyu, H. Li, K. Watanabe, T. Taniguchi *et al.*, "Signatures of tunable superconductivity in a trilayer graphene moiré superlattice," Nature **572**, 215–219 (2019).

[9]G. Chen, L. Jiang, S. Wu, B. Lyu, H. Li, B. L. Chittari, K. Watanabe, T. Taniguchi, Z. Shi, J. Jung *et al.*, "Evidence of a gate-tunable Mott insulator in a trilayer graphene moiré superlattice," Nat. Phys. **15**, 237–241 (2019).

[10]C. Shen, Y. Chu, Q. Wu, N. Li, S. Wang, Y. Zhao, J. Tang, J. Liu, J. Tian, K. Watanabe *et al.*, "Correlated states in twisted double bilayer graphene," Nat. Phys. **16**, 520–525 (2020).

[11]Y. Cao, D. Rodan-Legrain, O. Rubies-Bigorda, J. M. Park, K. Watanabe, T. Taniguchi, and P. Jarillo-Herrero, "Tunable correlated states and spin-polarized phases in twisted bilayer–bilayer graphene," Nature **583**, 215–220 (2020).

[12]G. W. Burg, J. Zhu, T. Taniguchi, K. Watanabe, A. H. MacDonald, and E. Tutuc, "Correlated insulating states in twisted double bilayer graphene," Phys. Rev. Lett. **123**, 197702 (2019).

[13]M. He, Y. Li, J. Cai, Y. Liu, K. Watanabe, T. Taniguchi, X. Xu, and M. Yankowitz, "Symmetry breaking in twisted double bilayer graphene," Nat. Phys. **17**, 26–30 (2021).

[14]M. Yankowitz, S. Chen, H. Polshyn, Y. Zhang, K. Watanabe, T. Taniguchi, D. Graf, A. F. Young, and C. R. Dean, "Tuning superconductivity in twisted bilayer graphene," Science **363**, 1059–1064 (2019).

[15]X. Lu, P. Stepanov, W. Yang, M. Xie, M. A. Aamir, I. Das, C. Urgell, K. Watanabe, T. Taniguchi, G. Zhang *et al.*, "Superconductors, orbital magnets and correlated states in magic-angle bilayer graphene," Nature **574**, 653–657 (2019).

[16]P. Stepanov, I. Das, X. Lu, A. Fahimniya, K. Watanabe, T. Taniguchi, F. H. L. Koppens, J. Lischner, L. Levitov, and D. K. Efetov, "Untying the insulating and superconducting orders in magic-angle graphene," Nature **583**, 375–378 (2020).

[17]A. L. Sharpe, E. J. Fox, A. W. Barnard, J. Finney, K. Watanabe, T. Taniguchi, M. A. Kastner, and D. Goldhaber-Gordon, "Emergent ferromagnetism near three-quarters filling in twisted bilayer graphene," Science **365**, 605–608 (2019).

[18]M. Serlin, C. L. Tschirhart, H. Polshyn, Y. Zhang, J. Zhu, K. Watanabe, T. Taniguchi, L. Balents, and A. F. Young, "Intrinsic quantized anomalous Hall effect in a moiré heterostructure," Science **367**, 900–903 (2020).

[19]C. Xu and L. Balents, "Topological superconductivity in twisted multilayer graphene," Phys. Rev. Lett. **121**, 087001 (2018).

[20]C.-C. Liu, L.-D. Zhang, W.-Q. Chen, and F. Yang, "Chiral spin density wave and $d + id$ superconductivity in the magic-angle-twisted bilayer graphene," Phys. Rev. Lett. **121**, 217001 (2018).

[21]M. Claassen, D. M. Kennes, M. Zingl, M. A. Sentef, and A. Rubio, "Universal optical control of chiral superconductors and Majorana modes," Nat. Phys. **15**, 766–770 (2019).

[22]L. Xian, D. M. Kennes, N. Tancogne-Dejean, M. Altarelli, and A. Rubio, "Multiflat bands and strong correlations in twisted bilayer boron nitride: Doping-induced correlated insulator and superconductor," Nano Lett. **19**, 4934–4940 (2019).

[23]K. Kim, A. DaSilva, S. Huang, B. Fallahazad, S. Larentis, T. Taniguchi, K. Watanabe, B. J. LeRoy, A. H. MacDonald, and E. Tutuc, "Tunable moiré bands and strong correlations in small-twist-angle bilayer graphene," Proc. Natl. Acad. Sci. U. S. A. **114**, 3364–3369 (2017).

[24]A. Kerelsky, L. J. McGilly, D. M. Kennes, L. Xian, M. Yankowitz, S. Chen, K. Watanabe, T. Taniguchi, J. Hone, C. Dean, A. Rubio, and A. N. Pasupathy, "Maximized electron interactions at the magic angle in twisted bilayer graphene," Nature **572**, 95–100 (2019).

[25]A. Kerelsky, C. Rubio-Verdú, L. Xian, D. M. Kennes, D. Halbertal, N. Finney, L. Song, S. Turkel, L. Wang, K. Watanabe, T. Taniguchi, J. Hone, C. Dean, D. N. Basov, A. Rubio, and A. N. Pasupathy, "Moiréless correlations in ABCA graphene," Proc. Natl. Acad. Sci. U. S. A. **118**, e2017366118 (2021).

[26]D. Halbertal, N. R. Finney, S. S. Sunku, A. Kerelsky, C. Rubio-Verdú, S. Shabani, L. Xian, S. Carr, S. Chen, C. Zhang, L. Wang, D. Gonzalez-Acevedo, A. S. McLeod, D. Rhodes, K. Watanabe, T. Taniguchi, E. Kaxiras, C. R. Dean, J. C. Hone, A. N. Pasupathy, D. M. Kennes, A. Rubio, and D. N. Basov, "Moiré metrology of energy landscapes in van der Waals heterostructures," Nat. Commun. **12**, 242 (2021).

[27]C. Rubio-Verdú, S. Turkel, Y. Song, L. Klebl, R. Samajdar, M. S. Scheurer, J. W. F. Venderbos, K. Watanabe, T. Taniguchi, H. Ochoa, L. Xian, D. Kennes, R. M. Fernandes, A. Rubio, and A. N. Pasupathy, "Moiré nematic phase in twisted double bilayer graphene," Nature Phys. **18**, 196–202 (2021).

[28]R. Bistritzer and A. H. MacDonald, "Moiré bands in twisted double-layer graphene," Proc. Natl. Acad. Sci. U. S. A. **108**, 12233–12237 (2011).

[29]G. Trambly de Laissardière, D. Mayou, and L. Magaud, "Localization of Dirac electrons in rotated graphene bilayers," Nano Lett. **10**, 804–808 (2010).

[30]J. M. B. Lopes dos Santos, N. M. R. Peres, and A. H. Castro Neto, "Continuum model of the twisted graphene bilayer," Phys. Rev. B **86**, 155449 (2012).

[31]L. Wang, E.-M. Shih, A. Ghiotto, L. Xian, D. A. Rhodes, C. Tan, M. Claassen, D. M. Kennes, Y. Bai, B. Kim *et al.*, "Correlated electronic phases in twisted bilayer transition metal dichalcogenides," Nat. Mater. **19**, 861–866 (2020).

[32]L. An, X. Cai, D. Pei, M. Huang, Z. Wu, Z. Zhou, J. Lin, Z. Ying, Z. Ye, X. Feng, R. Gao, C. Cacho, M. Watson, Y. Chen, and N. Wang, "Interaction effects and superconductivity signatures in twisted double-bilayer WSe$_2$," Nanoscale Horiz. **5**, 1309–1316 (2020).

[33]H. S. Arora, R. Polski, Y. Zhang, A. Thomson, Y. Choi, H. Kim, Z. Lin, I. Z. Wilson, X. Xu, J.-H. Chu *et al.*, "Superconductivity in metallic twisted bilayer graphene stabilized by WSe$_2$," Nature **583**, 379–384 (2020).

[34]L. Xian, M. Claassen, D. Kiese, M. M. Scherer, S. Trebst, D. M. Kennes, and A. Rubio, "Realization of nearly dispersionless bands with strong orbital anisotropy from destructive interference in twisted bilayer MoS$_2$," Nat. Commun. **12**, 5644 (2021).

[35]F. Wu, T. Lovorn, E. Tutuc, and A. H. MacDonald, "Hubbard model physics in transition metal dichalcogenide moiré bands," Phys. Rev. Lett. **121**, 026402 (2018).

[36]F. Wu, T. Lovorn, E. Tutuc, I. Martin, and A. H. MacDonald, "Topological insulators in twisted transition metal dichalcogenide homobilayers," Phys. Rev. Lett. **122**, 086402 (2019).

[37]M. Angeli and A. H. MacDonald, "Γ valley transition metal dichalcogenide moiré bands," Proc. Natl. Acad. Sci. U. S. A. **118**, e2021826118 (2021).

[38]M. H. Naik and M. Jain, "Ultraflatbands and shear solitons in moiré patterns of twisted bilayer transition metal dichalcogenides," Phys. Rev. Lett. **121**, 266401 (2018).

[39]E. C. Regan, D. Wang, C. Jin, M. I. Bakti Utama, B. Gao, X. Wei, S. Zhao, W. Zhao, Z. Zhang, K. Yumigeta, M. Blei, J. D. Carlström, K. Watanabe, T. Taniguchi, S. Tongay, M. Crommie, A. Zettl, and F. Wang, "Mott and generalized Wigner crystal states in WSe$_2$/WS$_2$ moiré superlattices," Nature **579**, 359–363 (2020).

[40]X. Qian, J. Liu, L. Fu, and J. Li, "Quantum spin Hall effect in two-dimensional transition metal dichalcogenides," Science **346**, 1344–1347 (2014).

[41]M. M. Scherer, D. M. Kennes, and L. Classen, "$\mathcal{N} = 4$ chiral superconductivity in moiré transition metal dichalcogenides," arXiv:2108.11406 [cond-mat.str-el] (2021).

[42]Y. Tang, L. Li, T. Li, Y. Xu, S. Liu, K. Barmak, K. Watanabe, T. Taniguchi, A. H. MacDonald, J. Shan *et al.*, "Simulation of Hubbard model physics in WSe$_2$/WS$_2$ moiré superlattices," Nature **579**, 353–358 (2020).

[43]M. Koshino, N. F. Yuan, T. Koretsune, M. Ochi, K. Kuroki, and L. Fu, "Maximally localized Wannier orbitals and the extended Hubbard model for twisted bilayer graphene," Phys. Rev. X **8**, 031087 (2018).

[44]H. Pan, F. Wu, and S. Das Sarma, "Band topology, Hubbard model, Heisenberg model, and Dzyaloshinskii-Moriya interaction in twisted bilayer WSe$_2$," Phys. Rev. Res. **2**, 033087 (2020).

[45]J. Zang, J. Wang, J. Cano, and A. J. Millis, "Hartree-Fock study of the moiré Hubbard model for twisted bilayer transition metal dichalcogenides," Phys. Rev. B **104**, 075150 (2021).

[46]Y. Iqbal, W.-J. Hu, R. Thomale, D. Poilblanc, and F. Becca, "Spin liquid nature in the Heisenberg $J_1 - J_2$ triangular antiferromagnet," Phys. Rev. B **93**, 144411 (2016).

[47]S. Hu, W. Zhu, S. Eggert, and Y.-C. He, "Dirac spin liquid on the spin-1/2 triangular Heisenberg antiferromagnet," Phys. Rev. Lett. **123**, 207203 (2019).

[48]Z. Zhu and S. R. White, "Spin liquid phase of the $S = \frac{1}{2}$ $J_1 - J_2$ Heisenberg model on the triangular lattice," Phys. Rev. B **92**, 041105 (2015).

[49]Y. Shimizu, K. Miyagawa, K. Kanoda, M. Maesato, and G. Saito, "Spin liquid state in an organic Mott insulator with a triangular lattice," Phys. Rev. Lett. **91**, 107001 (2003).

[50] A. Szasz, J. Motruk, M. P. Zaletel, and J. E. Moore, "Chiral spin liquid phase of the triangular lattice Hubbard model: A density matrix renormalization group study," Phys. Rev. X **10**, 021042 (2020).

[51] S. R. White, "Density matrix formulation for quantum renormalization groups," Phys. Rev. Lett. **69**, 2863–2866 (1992).

[52] I. P. McCulloch, "Infinite size density matrix renormalization group, revisited," arXiv:0804.2509 [cond-mat.str-el] (2008).

[53] V. Zauner, D. Draxler, L. Vanderstraeten, M. Degroote, J. Haegeman, M. M. Rams, V. Stojevic, N. Schuch, and F. Verstraete, "Transfer matrices and excitations with matrix product states," New J. Phys. **17**, 053002 (2015).

[54] Z. Zhang, Y. Wang, K. Watanabe, T. Taniguchi, K. Ueno, E. Tutuc, and B. J. LeRoy, "Flat bands in twisted bilayer transition metal dichalcogenides," Nat. Phys. **16**, 1093–1096 (2020).

[55] J. M. Luttinger and L. Tisza, "Theory of dipole interaction in crystals," Phys. Rev. **70**, 954–964 (1946).

[56] C. Liu, R. Yu, and X. Wang, "Semiclassical ground-state phase diagram and multi-Q phase of a spin-orbit-coupled model on triangular lattice," Phys. Rev. B **94**, 174424 (2016).

[57] Note that for a BKT transition, the specific heat T_{peak} does not mark the location of the phase transition but instead slightly overestimates it, e.g., $T_{peak} \sim 1.1 - 1.2 T_{BKT}$ for the triangular lattice XXZ model.[58,78]

[58] L. Capriotti, R. Vaia, A. Cuccoli, and V. Tognetti, "Phase transitions induced by easy-plane anisotropy in the classical Heisenberg antiferromagnet on a triangular lattice: A Monte Carlo simulation," Phys. Rev. B **58**, 273–281 (1998).

[59] J. Reuther and P. Wölfle, "$J_1 - J_2$ frustrated two-dimensional Heisenberg model: Random phase approximation and functional renormalization group," Phys. Rev. B **81**, 144410 (2010).

[60] J. Reuther and R. Thomale, "Functional renormalization group for the anisotropic triangular antiferromagnet," Phys. Rev. B **83**, 024402 (2011).

[61] Y. Iqbal, R. Thomale, F. Parisen Toldin, S. Rachel, and J. Reuther, "Functional renormalization group for three-dimensional quantum magnetism," Phys. Rev. B **94**, 140408 (2016).

[62] M. L. Baez and J. Reuther, "Numerical treatment of spin systems with unrestricted spin length S: A functional renormalization group study," Phys. Rev. B **96**, 045144 (2017).

[63] J. Thoenniss, M. K. Ritter, F. B. Kugler, J. von Delft, and M. Punk, "Multiloop pseudofermion functional renormalization for quantum spin systems: Application to the spin-$\frac{1}{2}$ kagome Heisenberg model," arXiv:2011.01268 [cond-mat.str-el] (2020).

[64] F. L. Buessen, D. Roscher, S. Diehl, and S. Trebst, "Functional renormalization group approach to SU(N) Heisenberg models: Real-space renormalization group at arbitrary N," Phys. Rev. B **97**, 064415 (2018).

[65] Recently, an advanced "multi-loop" truncation scheme has been successfully employed within the pf-FRG,[63,74] improving on certain aspects of the Katanin truncation. Since the respective one and higher loop ground state phase diagrams were, however, qualitatively the same, we refrain from performing higher loop calculations in this work to reduce the numerical effort involved in treating the off-diagonal DM interaction in combination with breaking of C_6 symmetry.

[66] We use bond dimension 3600 for Figs. 5(b), 5(c), 5(e), and 5(f) while using bond dimensions 3600 and 5000 for extrapolating[79] the non-vanishing m^z in Fig. 5(d).

[67] M. Koshino and Y.-W. Son, "Moiré phonons in twisted bilayer graphene," Phys. Rev. B **100**, 075416 (2019).

[68] I. Maity, M. H. Naik, P. K. Maiti, H. R. Krishnamurthy, and M. Jain, "Phonons in twisted transition-metal dichalcogenide bilayers: Ultrasoft phasons and a transition from a superlubric to a pinned phase," Phys. Rev. Res. **2**, 013335 (2020).

[69] M. Ye and A. V. Chubukov, "Quantum phase transitions in the Heisenberg $J_1 - J_2$ triangular antiferromagnet in a magnetic field," Phys. Rev. B **95**, 014425 (2017).

[70] H. Nakano and T. Sakai, "Magnetization process of the spin-1/2 triangular-lattice Heisenberg antiferromagnet with next-nearest-neighbor interactions—Plateau or nonplateau," J. Phys. Soc. Jpn. **86**, 114705 (2017).

[71] T. Okubo, S. Chung, and H. Kawamura, "Multiple-q states and the skyrmion lattice of the triangular-lattice Heisenberg antiferromagnet under magnetic fields," Phys. Rev. Lett. **108**, 017206 (2012).

[72] M. Akram, H. LaBollita, D. Dey, J. Kapeghian, O. Erten, and A. S. Botana, "Moiré skyrmions and chiral magnetic phases in twisted CrX$_3$ (X = I, Br, and Cl) bilayers," Nano Lett. **21**, 6633–6639 (2021).

[73] M.-H. Zare and H. Mosadeq, "Spin liquid in twisted homobilayers of group-VI dichalcogenides," Phys. Rev. B **104**, 115154 (2021).

[74] D. Kiese, T. Mueller, Y. Iqbal, R. Thomale, and S. Trebst, "Multiloop functional renormalization group approach to quantum spin systems," arXiv:2011.01269 [cond-mat.str-el] (2021).

[75] J. Hauschild and F. Pollmann, "Efficient numerical simulations with tensor networks: Tensor network Python (TeNPy)," SciPost Physics Lecture Notes 5, 2018.

[76] Jülich Supercomputing Centre, "JURECA: Modular supercomputer at Jülich Supercomputing Centre," J. Large-Scale Res. Facil. **4**, A132 (2018).

[77] Jülich Supercomputing Centre, "JUWELS: Modular tier-0/1 supercomputer at the Jülich Supercomputing Centre," J. Large-Scale Res. Facil. **5**, A171 (2019).

[78] R. Gupta and C. F. Baillie, "Critical behavior of the two-dimensional XY model," Phys. Rev. B **45**, 2883–2898 (1992).

[79] S. R. White and A. L. Chernyshev, "Neél order in square and triangular lattice Heisenberg models," Phys. Rev. Lett. **99**, 127004 (2007).